Interplay between medial nuclear stalling and lateral cellular flow underlies cochlear duct spiral morphogenesis

Mamoru Ishii[1], Tomoko Tateya[2], Michiyuki Matsuda[1,3], Tsuyoshi Hirashima*[3,4]

1. Laboratory of Bioimaging and Cell Signaling, Graduate School of Biostudies, Kyoto University
2. Department of Speech and Hearing Sciences and Disorders, Faculty of Health and Medical Sciences, Kyoto University of Advanced Science
3. Department of Pathology and Biology of Diseases, Graduate School of Medicine, Kyoto University
4. Japan Science and Technology Agency, PRESTO

Keywords: Differential growth, FRET imaging, Interkinetic nuclear migration, MAPK/ERK, Mathematical model, Morphogenesis, Spiral pattern formation

***Corresponding author:** Tsuyoshi Hirashima, Ph.D

Graduate School of Biostudies, Kyoto University
Yoshida-Konoe-cho, Sakyo-ku, Kyoto 606-8501, Japan
Phone: +81-75-753-9450, Fax: +81-75-753-4655
hirashima.tsuyoshi2m@kyoto-u.ac.jp

Abstract

A notable example of spiral architecture in organs is the mammalian cochlear duct, where the duct morphology is critical for hearing function. Molecular genetics has revealed the necessary signaling molecules for the formation of spirals in organs, but it remains unclear how cellular dynamics generate bending and coiling of the cochlear duct during development. Here we show two modes of multicellular dynamics underlying the morphogenetic process by combining deep tissue live-cell imaging, Förster resonance energy transfer (FRET)-based quantitation, and mathematical modeling. First, surgical separation of the cochlear duct revealed that bending forces reside primarily in the medial side of the duct. In the medial pseudostratified epithelium, we found that nuclei stall at the luminal side during interkinetic nuclear migration, which would cause the extension of the luminal side, thereby bending the duct. Second, long-term organ-scale FRET imaging of extracellular signal-regulated kinase (ERK) activity showed that helical ERK activation waves propagate from the duct tip concomitant with the reverse multicellular flow in the lateral side of the duct, resulting in advection-based duct elongation. We propose an interplay of distinct multicellular behaviors underpinning spiral morphogenesis in the developing cochlear duct.

Introduction

Spiral shapes are a widely occurring motif in many varied biological tissues and organisms, including shells, horns, and plants, but how spiral shapes form has remained unclear (Thompson, 1942). The general principle of spiral formation is differences in growth rate between the outer and inner tissue of the extending organ, with the growth rate of the outer tissue being faster than that of the inner one, which has been theoretically and experimentally demonstrated in shells and plants (Johnson et al., 2019; Raup and Michelson, 1965; Smyth, 2016; Wada and Matsumoto, 2018). The cellular processes causing this differential tissue growth are different in each organ (Johnson et al., 2019; Saffer et al., 2017), and so identifying the organ-specific mechanisms underlying these differential tissue growth rates is crucial to understanding the developmental process of spiral morphogenesis.

An example of a spiral organ is the mammalian cochlear duct, which is a tonotopically organized auditory organ in the inner ear (Fig. 1A). During murine development, the cochlear duct, composed of epithelial cells, elongates, bends, and coils to form a spiral. The molecular basis for the morphogenesis of the cochlear duct has been the subject of several previous studies. Gene knockout studies have clarified that the elongation of the cochlear duct requires sonic hedgehog (SHH) signaling from the cochleovestibular ganglion in the conical central axis of the cochlea (Bok et al., 2013; Liu et al., 2010; Tateya et al., 2013), fibroblast growth factor (FGF) signaling of epithelial cells (Pauley et al., 2003; Pirvola et al., 2000; Urness et al., 2018, 2015), and non-canonical Wnt–planar cell polarity (PCP) signaling of prosensory cells (Mao et al., 2011; Montcouquiol and Kelley, 2020; Qian et al., 2007; Saburi et al., 2008; Wang et al., 2005). Deletion of *Shh* expression leads to a shortening of the cochlear duct and a significant decrease in cell proliferation exclusively at the base region (Bok et al., 2013). In *Fgf10* null mutant mice, the cochlear duct is remarkably shorter, but cell proliferation is unaffected (Urness et al., 2015), suggesting that cell proliferation and other cellular processes regulate ductal outgrowth. From embryonic day (E) 14.5 onwards, the mediolateral active migration of prosensory cells, during which these cells intercalate radially with their neighbors (known as convergent extension), contributes to longitudinal duct extension in a Wnt–PCP pathway-dependent manner (Chen et al., 2002; Cohen et al., 2019; Driver et al., 2017; Yamamoto et al., 2009). This cell intercalation drives ductal elongation; however, it cannot explain the asymmetrical morphogenetic mode underlying the duct bending before E14.5. Although the underlying signaling pathways are well characterized, the physical cellular mechanisms underlying spiral morphogenesis of the cochlear duct remain elusive. In the present study, we

aimed to identify the multicellular dynamics giving rise to the bending and coiling of the developing cochlear duct using a combination of live cell-imaging, FRET quantitation, and mathematical modeling.

Results

The medial epithelial layer causes cochlear duct bending

Mediolateral asymmetry characterizes the spiral form of the cochlear duct (Fig. 1A). We therefore first examined the force balance between the medial and the lateral tissue by surgically separating the cochlear duct along the lateral side of the hair cells (Fig. 1B); the medial side included Kölliker's organ and the prosensory domain, and the lateral side included the outer sulcus after separation. This manipulation led to the release of the mechanical stress affected mutually between the medial and the lateral tissue, enabling us to inspect the internal stresses of local tissues. The separated medial tissue curled much more after separation than before, while the lateral tissue was relatively uncurled (Fig. 1C and Mov. 1), indicating that active bending force are applied from the medial side, but not from the lateral side.

We next examined the morphology of the developing cochlear duct from E12.5 to E14.5 by staining an epithelial marker, E-cadherin, and performing organ-scale 3D imaging. During this developmental period, the cochlear duct elongates and coils without changes to the mediolateral width (Fig. 1D). The curvature and thickness of the epithelial layer are significantly larger on the medial side than on the lateral side in a horizontal section of the roof-floor axis (Fig. 1D). Hereafter, we refer to the epithelial layers on the medial and lateral sides as the medial and lateral epithelial layers (MEL and LEL), respectively (Fig. 1E). Morphological quantification revealed that the curvature and thickness of the MEL are highest at a point more than 100 μm away from the tip of the duct along the MEL (Fig. 1F and S1). In contrast, the curvature and thickness of the LEL remain constant (Fig. 1F and S1). These observations prompted us to explore the structure and dynamics of the MEL at single cell resolution.

Zooming in the epithelial layer clarified that most of the nuclei in the LEL align within a few nucleus diameters of each other (~20 μm) (Fig. 1G, left). However, nuclei in the MEL distribute broadly across a ~50 μm range, and mitotic cell rounding only occurs on the luminal side of the MEL (Fig. 1G, right). We also found that nuclei that stained positive for the M phase marker phospho-histone H3 (pHH3) were localized only on the luminal side of the epithelial

layers, while nuclei in the S phase cells labeled with a short pulse of ethynyl deoxyuridine (EdU) were distributed predominantly on the basal side (Fig. 1H). Mosaic cell labeling revealed that single cell bridges extended between the luminal and basal edges of the MEL via long protrusions (Fig. 1I), clearly indicating that the MEL is a proliferative pseudostratified epithelial tissue.

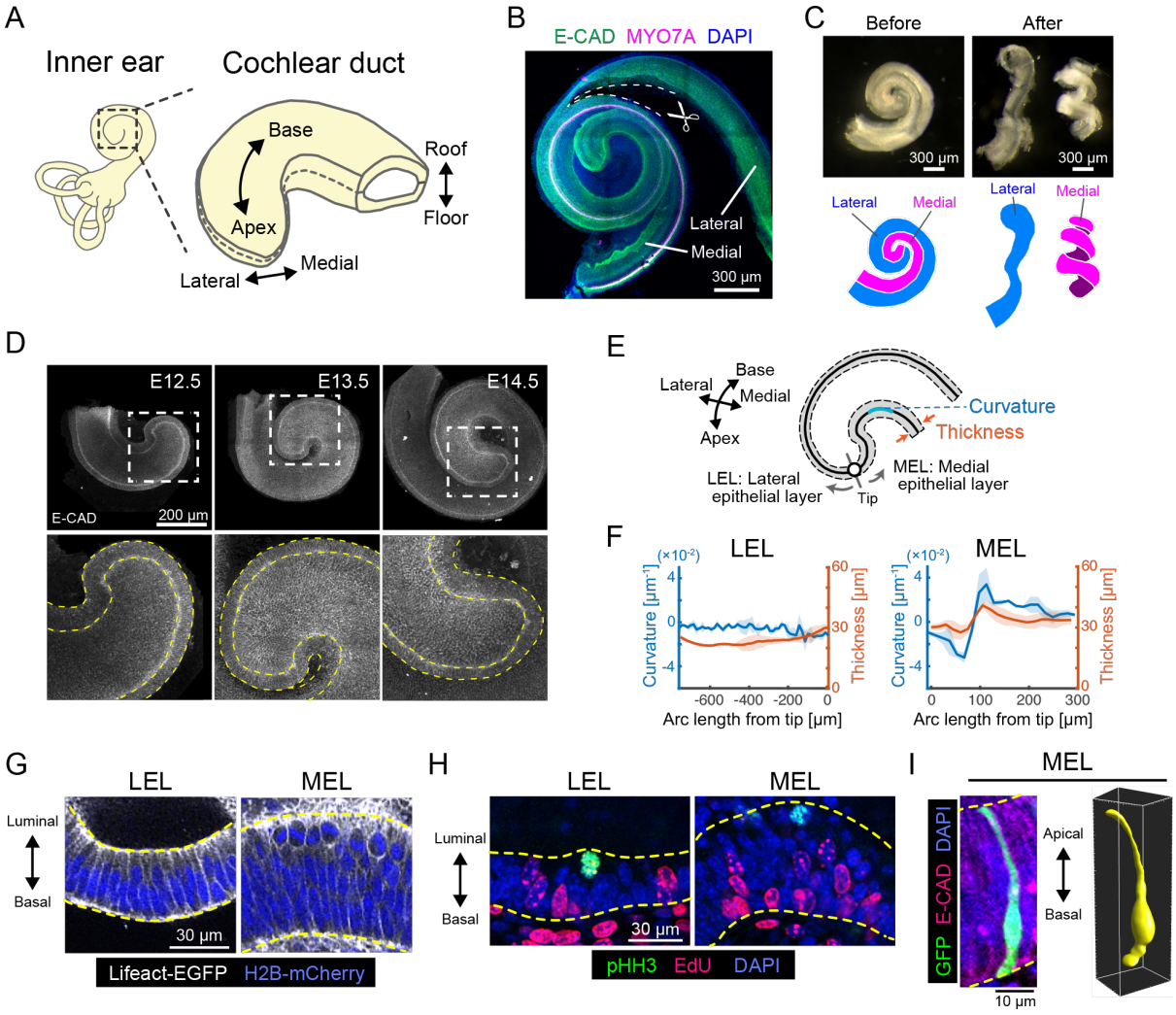

Figure 1 The pseudostratified medial epithelial layer curves in the cochlear duct
(A) Schematic diagrams showing the tissue axis and labels of the cochlear duct. (B) Immunofluorescence image of anti-E-cadherin (green) and anti-Myosin VIIA, a marker for sensory hair cells (magenta), with nuclear counterstaining using DAPI (blue) in the cochlea at E17.5 during tissue separation, with cuts represented by dashed lines. N=3 was confirmed. Scale bar, 300 μm. (C) Images of the cochlear duct before and after tissue separation. Stereomicroscope images (upper) and the corresponding illustrations of the lateral (blue, left) and medial (magenta, right) layers. N=3 was confirmed. Scale bar, 300 μm. (D) Immunofluorescence images of anti-E-cadherin staining in the murine developing cochlea. The lower rows are magnified images of the dotted squares in the upper rows. Yellow dotted lines represent the edges of the epithelial layer. Scale bar, 200 μm. (E) Schematic diagram showing

regions used for morphological quantification. (F) Curvature and thickness as a function of the arc length from the tip along the lateral epithelial layer (LEL, left) and the medial epithelial layer (MEL, right) at E12.5. Mean ± standard deviation (s.d.) N=3. (G) Images of Lifeact-EGFP (white) and H2B-mCherry (blue) showing cell shape and nuclear position in the LEL and MEL. Yellow dotted lines represent the luminal and basal edges. Scale bar, 30 μm. (H) Fluorescence labeling images of anti-pHH3 (green) and EdU (magenta) with nuclear counterstaining using DAPI (blue) in the LEL and MEL. Yellow dotted lines represent the luminal and basal edges. Scale bar, 30 μm. (I) Fluorescence image of GFP transfected cells labelling single cells (green) and anti-E-cadherin (magenta) with nuclear counterstaining using DAPI (blue) in the MEL (left) and the corresponding 3D rendered image (right). Yellow dotted lines on the left represent the luminal and basal edges. Scale bar, 10 μm.

Luminal nuclear stalling promotes MEL bending

We next focused on the cellular dynamics in the MEL with a two-photon microscope. For live imaging of the MEL, the outer cartilaginous shell that will develop into the bony labyrinth was completely removed to expose the cochlear duct prior to *ex vivo* culture. We used a reporter mouse line ubiquitously expressing fluorescence proteins localized in the cytoplasm, allowing us to recognize the nuclei as the regions without fluorescence, as well as the luminal and basal edges of MEL in the pseudostratified epithelium. We observed differences in the nuclear movement between the flat region proximal to the tip of the apex and the curved region distal to the tip of apex (Fig. 2A, Mov. 2). The nuclei moved to the luminal edge of the epithelial layer before cell division, and after cell division the daughter nuclei returned to the basal side in the flat region (Fig. 2B). In the curved region, however, the cell nuclei remained at the luminal side even after cell division (Fig. 2C). To make this difference clearer, we tracked the nuclei and quantified their distance from the luminal edge at 3 hours after nuclear division. After classifying the tissue into two categories – flat and curved – based on the half-maximal curvature (Fig. 2D), fewer nuclei move to the basal side in the curved region than in the flat region (Fig. 2D'), suggesting that there are two different modes of luminal-basal nuclear movement in the MEL, depending on the distance from the duct tip. In addition, we examined two angles of cell division orientation, φ and θ, in the 3D polar coordinates from the live imaging data, with φ and θ representing the zenith and azimuth angle, respectively (Fig. 2E). The φ angle was between 0° to 45°, indicating that cell division mostly occurs in parallel to the luminal surface of the MEL (Fig. 2F). The distribution of θ shows that most cells divide along the apex-base axis rather than along the roof-floor axis (Fig. 2G), suggesting that the orientation of cell division contributes to the apex-base local expansion of the luminal side of the MEL.

Luminal-basal nuclear movement in the flat region exhibits the behavior known as interkinetic nuclear migration (IKNM), which has been observed in various pseudostratified epithelia (Grosse et al., 2011; Kosodo et al., 2011; Meyer et al., 2011; Norden et al., 2009; Sauer, 1935). During this process, nuclei at the basal side move close to the luminal surface prior to mitosis, and the daughter nuclei move back to the basal side, which results in even growth within the epithelial layer (Fig. 2H, upper). This mode of nuclear migration would not necessarily result in bending of the epithelial tissue. In contrast, lack of basalward movement during IKNM, which we refer to as 'luminal nuclear stalling' hereafter, results in asymmetric one-way flux of nuclei from the basal side to the luminal surface of the layer, which results in local cell crowding and expansion due to the division occurring at the luminal side (Fig. 2H, lower). This asymmetrical IKNM, along with oriented cell division, may contribute to differential growth between the luminal and basal sides of the MEL, and thus cause the physical bending of the MEL.

To test this possibility, we built a cell-based mechanical model and examined whether nuclear movements affect the curvature of an epithelial layer. Single epithelial cells in the layer were represented as polygons with vertices consisting of the luminal and basal edges, which could deform according to the cell cycle-dependent nuclear position, based on mechanical interactions between neighboring cells (Fig. 2I). We then introduced a parameter $\boldsymbol{\gamma}$ controlling the degree of basalward movement after IKNM – the nucleus moves to the basal edge when $\boldsymbol{\gamma = 1}$ and stays at the luminal side when $\boldsymbol{\gamma = 0}$. Our mathematical simulation demonstrated that the curvature of the epithelial layer monotonically decreases as a function of $\boldsymbol{\gamma}$ (Fig. S2A), which supports our observation that luminal nuclear stalling mechanically contributes to bending of the epithelial layer. We used an *in silico* experiment to predict that cell cycle arrest at the S-phase entry would decrease the curvature of the MEL (Fig. 2J, 2K, and Mov. 3). This prediction was validated by treating explant cochlea with the DNA synthesis inhibitor Mitomycin C. After 1 day of treatment with 10 μM Mitomycin C, EdU-positive S phase cells were no longer detected in the cochlea (Fig. S2B). Under these conditions, the amount of curvature along the MEL was significantly decreased in the curved region (Fig. 2L and 2M), which is consistent with the model prediction. These results corroborate our hypothesis that luminal nuclear stalling after luminal mitosis promotes MEL bending.

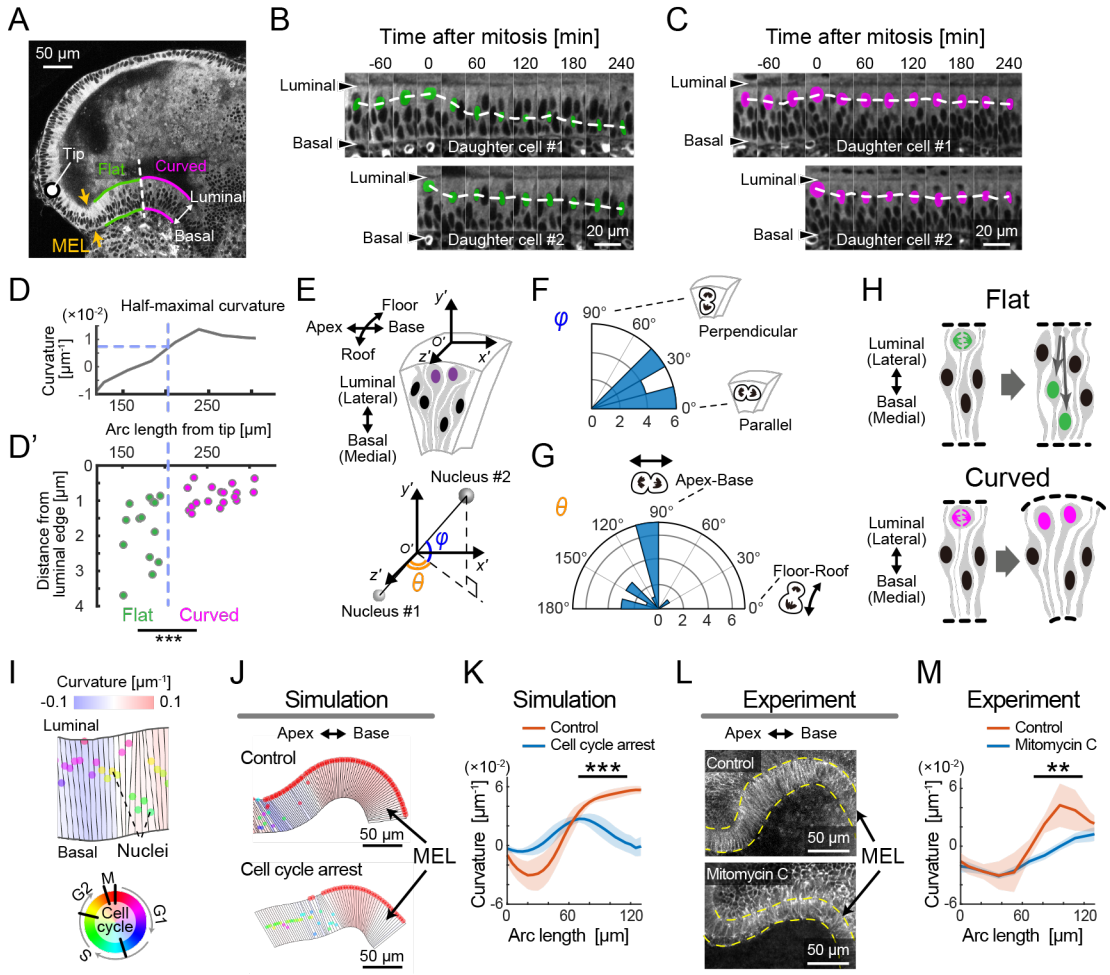

Figure 2 Live imaging and mathematical modelling demonstrate that luminal nuclear stalling promotes MEL bending via luminal-basal differential growth

(A) Image of a section of an E14.5 cochlea in cytoplasmic reporter mice (CFP channel of ERK-FERT mice). The MEL was classified into flat (green) and curved (magenta) regions and the boundary between the flat and curved regions is indicated by a dotted line. The circle indicates the duct tip. Scale bar, 50 μm. (B, C) Kymographic images of the flat region (B) and the curved region (C). Dotted lines denote a change in position of manually marked nuclei over time. Scale bars, 20 μm. (D, D') For 16 nuclear divisions that could be tracked, the distance from the luminal edge 3 hours after nuclear division was plotted over the arc length from the tip (D') together with the MEL curvature (D). At half-maximal curvature (D), the samples in (D') were classified into two groups, i.e., flat (n=14) and curved (n=18). Mann–Whitney U test, p=0.00038. (E) Nuclear division orientation is represented by two angles, φ and θ, in the polar coordinate O'. (F, G) Angle distribution of φ and θ. n=16. Rayleigh test, p=0.00096 for (F) and p=0.15 for (G). (H) Schematics for the expected morphology depending on the mode of nuclear movement. IKNM would lead to the flat (upper) and asymmetric IKNM would lead to the curved (lower). (I) Virtual epithelial layer in the model simulation. The colored circles denote nuclei with the cell cycle state represented in the bottom. (J, K) Model prediction in the cell cycle arrest before S phase entry in the growing virtual MEL. Representative images (J) and the curvature over the arc length (K). Mean ± s.d. N=10. Mann–Whitney U test, p<0.001. Scale bar, 50 μm. (L, M) The effect of mitomycin C treatment. Representative images of resultant cochlear duct immunostaining of anti-E-cadherin (J) and the curvature over the arc length (M).

Mean ± s.d. N=3. Mann–Whitney U test, p=0.0017. Scale bar, 50 μm.

Spatial heterogeneity of cell proliferation suggests cellular inflow to the lateral side of the apex to realize cochlear bending

One plausible mechanism for achieving the spiral morphology of the cochlear duct is MEL-driven differential growth, but another possibility is that cell proliferation might occur at a faster rate on the lateral side than on the medial side. To address this, we examined the spatial distribution of proliferating cells within 30 min of labeling of EdU on the roof and floor side of the cochlear duct (Fig. 3A and 3B). For quantification, the image domain of the cochlear duct was divided into interrogation regions and the averaged fluorescence intensity of labelled EdU was measured within each region (Fig. 3C). On the floor side, EdU-positive cells were more abundant in the medial side than in the lateral side around the apex (arrows, Fig. 3B and 3D, left). However, on the roof side of the cochlear duct, EdU-positive cells were distributed evenly, with slightly fewer cells at the base than at the apex and without a significant bias along the mediolateral axis (Fig. 3B and 3D, right). These observations negate the possibility that cell proliferation rates on the lateral side of the cochlear duct could drive mediolateral differential tissue growth and cause duct bending. The spatial map of EdU intensity shows that cell proliferation rates were higher in the floor-base region (arrowheads, Fig. 3B and 3D, left). Supposing that cell proliferation is the main driver of local tissue growth, the higher volumetric growth observed in the medial side than in the lateral side would contribute to the duct bending inward at the lateral side, which contradicts the innate cochlear morphogenesis. We thus hypothesized that the cells in the lateral side of the growing apex may be supplied by proliferation ‘hot spot’ in the basal region of the cochlear duct, which could resolve the observed mismatch between tissue growth rates in the medial and lateral sides of the duct.

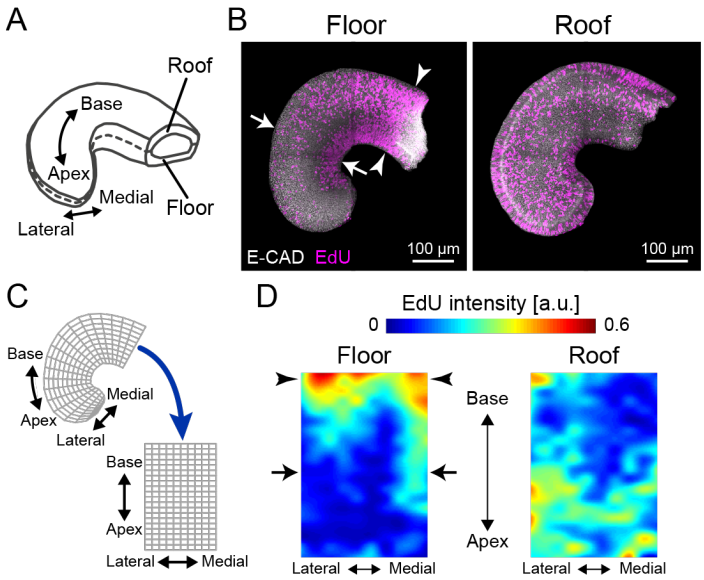

Figure 3 Cell proliferation mapping suggests cellular inflow to the lateral side of the cochlear duct apex to realize cochlear bending

(A) Schematic of tissue axis of the cochlear duct. (B) Maximum projection images of stained anti-E-cadherin (white) and EdU (magenta) in the roof and floor region of cochlear duct at E12.5. Representative images showing EdU signals in the cochlear duct are shown. Arrows indicate the region of EdU signal gradient from the medial to the lateral side of the duct. Arrowheads indicate the base region where the EdU intensity is concentrated. Scale bar, 100 μm. (C) Regional mapping from irregular grids in the cochlear duct to regular grids. (D) Heat map of EdU intensity in the roof and floor region of the duct. Arrows and arrowheads are the same as in (B). N=3 was confirmed.

Retrograde helical ERK activation waves drive base-to-apex multicellular flow

How are cells supplied from the base of the cochlear duct to the lateral side? Earlier studies reported that FGF signaling is critical for cochlear duct outgrowth (Pirvola et al., 2000; Urness et al., 2015). We therefore focused on ERK MAP kinase, a downstream kinase in the FGF signaling pathway, and used a reporter mouse line that ubiquitously expresses a Förster resonance energy transfer (FRET)-based biosensor for ERK activity in the cytosol (Harvey et al., 2008; Komatsu et al., 2018, 2011). 3D FRET imaging using two-photon microscopy revealed that ERK is preferentially activated in the lateral-roof side of the cochlear duct, including the outer sulcus and stria vascularis (Fig. 4A, 4A', and Mov. 4), which is consistent with the previously reported distribution of *Fgfr2* expression (Urness et al., 2015).

For continuous observation during ductal outgrowth, we established an explant culture method in which the capsule above the duct tip was partially removed, allowing 3D organ-scale long-term imaging of ERK activity. Surprisingly, the time-lapse images of the cochlea

dissected at E12.5 revealed that ERK activation propagates intercellularly as oscillatory waves from the apex to the base of the floor side (Fig. 4B and Mov. 5), while ERK is constitutively activated around the ductal tip of the roof side (Fig. S3A and S3B). We next quantified multicellular tissue flow by particle image velocimetry (PIV) at the supra-cellular (4–5 cell length) scale, and found that cells coherently move as clusters of ~100 μm diameter from the base to the apex of the floor side, again as oscillatory waves, and similarly to the ERK activation waves of the floor side (Fig. 4C and Mov. 5). In the roof side, the multicellular tissue flows directly toward the direction of elongation around the duct tip (Fig. S3C). Kymography of ERK activity along the apex-base line of the lateral-floor side (Fig. 4D) shows oscillatory retrograde ERK activity waves (Fig. 4E and Fig. S3D), which proceed at a speed of 0.42 ± 0.078 μm min^{-1} (mean ± standard deviation) in space-fixed coordinates (Fig. 4F).

Since ERK activation can be induced by cell extension during collective cell migration (Hino et al., 2020), we further calculated the ERK activity rate, i.e., the time derivative of ERK activity, and the extension-shrinkage rate, i.e., the local tissue strain rate along the apex-base line, by using time-series data of ERK activity and PIV speed, respectively (Fig. S3E). We found that both the ERK activity rate and the extension-shrinkage rate oscillate across the time course (Figure 4G). Moreover, cross-correlation analysis revealed that the local tissue deformation, represented by the extension-shrinkage rate, precedes ERK activity changes by 24 min on average (Fig. 4H). This is consistent with a regime of mechano-chemical coupling for collective cell migration: extension-triggered ERK activation promotes cell contraction, pulling the neighboring cells, which eventually evokes another round of ERK activation in the neighboring cells (Boocock et al., 2020; Hino et al., 2020). The observed lag time between the ERK activity rate and the extension-shrinkage rate can be reproduced using a minimal mathematical model of the mechano-chemical coupling, but not by an uncoupling model under which the ERK activation waves regulate the cell deformation unidirectionally, supporting the plausibility of mechano-chemical coupling rather than an uncoupling regime (Fig. S4). The role played by ERK was confirmed by treating the cochlear duct with an inhibitor of the upstream kinase MEK, PD0325901. Treatment with the MEK inhibitor at 1 μM resulted in a significant decrease of the tissue flow speed (Fig. 4I) as well as ERK inactivation (Fig. S3F), corroborating that ERK activation waves contribute to the base-to-apex multicellular tissue flow.

Finally, we extended the analysis to 3D dynamics of ERK activity and cell movement in the developing cochlear duct. Surface rendering of the ERK activity map in the cytosol indicated that ERK activity peaks shift from the apex-roof to the base-floor in the lateral side

of the cochlear duct (Fig. 4J and Mov. 6). Concomitantly with helical ERK activity waves, coherent cell movements can be observed from the base-floor to the apex-roof in the opposite direction to the ERK waves (Mov. 6). This observation strongly suggests that ERK-mediated helical collective cell movement could drive 3D duct coiling underlying the spiral morphogenesis of the cochlear duct (Fig. 4K).

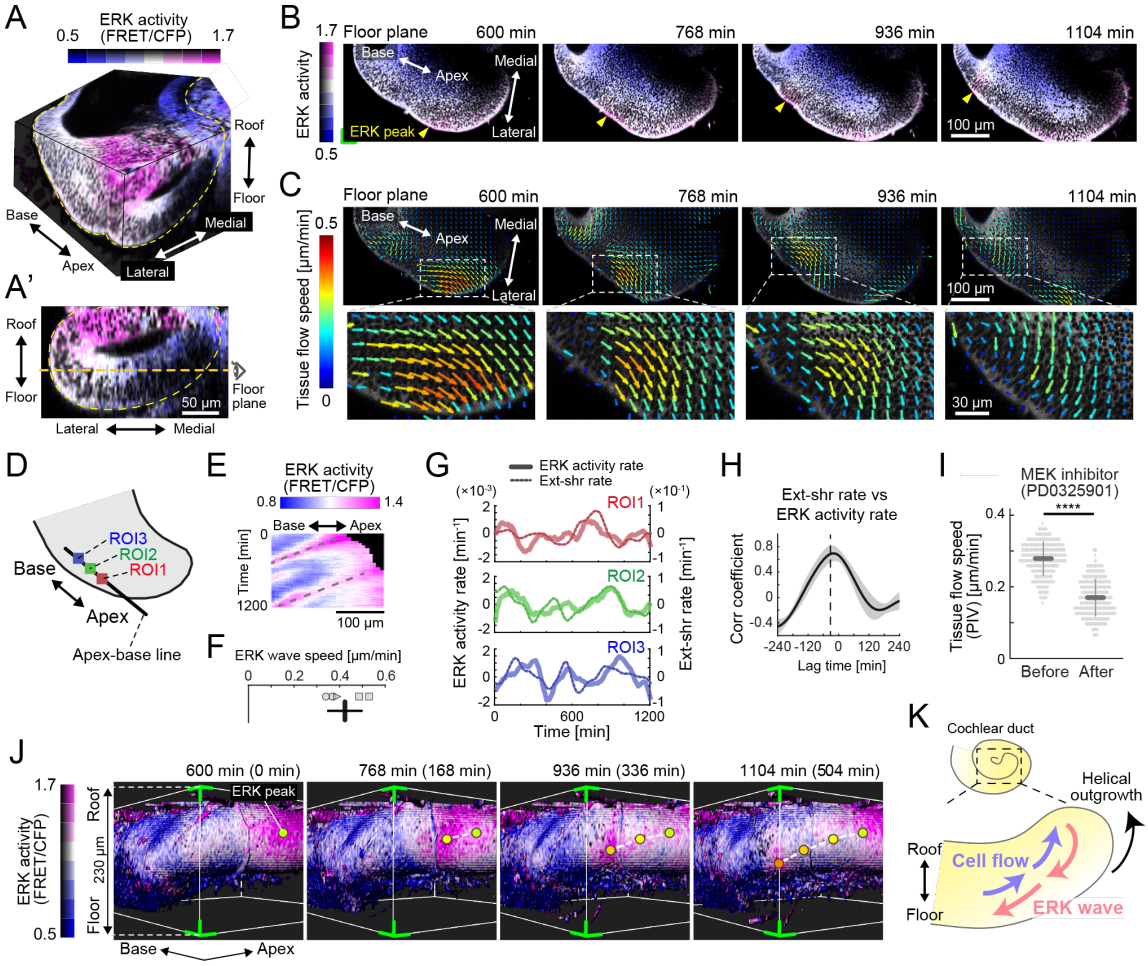

Figure 4 Retrograde helical ERK activation waves drive base-to-apex multicellular flow
(A) 3D ERK activity map in the cochlear duct at E12.5. (A') Cross section view (medial-lateral and roof-floor plane) of (A). Orange dotted line indicates the floor plane shown in (B) and (C). Scale bar, 50 µm. (B) Time-lapse snapshots of ERK activity maps in the floor plane. Time indicates the elapsed time of live imaging. Yellow arrowheads indicate the ERK activity peak. Scale bar, 100 µm. (C) Time-lapse snapshots of tissue flow speed obtained by PIV in the floor plane. Scale bar, 100 µm. (D) Schematic diagram showing the axis, the apex-base line for kymography, and regions of interests (ROIs). (E) Representative kymograph of ERK activity. The horizontal axis indicates the position on the apex-base line shown in (D) and the vertical axis indicates the elapsed time of live imaging. Dotted lines represent oscillatory waves from the apex to the base. Scale bar, 100 µm. (F) ERK wave speed with mean and s.d. n=5 from

N=3. (G) Time-series ERK activity rate and extension-shrinkage rate in representative 3 different ROIs. (H) Cross-correlation between the extension-shrinkage rate and ERK activity rate. n=12. Mean ± s.d. (I) Tissue flow speed before and after MEK inhibitor PD0325901 treatment at 1 μM. n=285 from N=3. Two-sample t-test, $p<0.001$. (J) Time-lapse snapshots of surface rendered ERK activity maps in the cochlear duct at E12.5. The green corners correspond to the green corner on the images shown in (B) and viewed from the left-bottom corner of (B). Circles indicate the position of ERK activity peaks and the connecting dotted lines indicate a trace of the peak shift. The time scale is the same as in (B). (K) Schematics for the ERK activity waves and cell flow.

Discussion

Previous genetic studies have revealed the molecular basis of cochlear duct elongation during development, but have been unable to explain the physical mechanisms by which the duct bends because of its severe phenotype (Bok et al., 2013; Groves and Fekete, 2012; Urness et al., 2018, 2015). Motivated by these earlier studies, we have visualized the cochlear duct development by two-photon microscopy and found that nuclei moving from the basal side stall at the luminal side after cell division, which gives rise to bending via differential tissue growth between the luminal and basal sides of MEL. We also elucidated that coherent cellular flow occurs from the base to the apex exclusively in the lateral wall of the growing cochlear duct, which is accompanied by retrograde ERK activation waves. Thus, our long-term deep tissue imaging has illuminated unprecedented dynamics of cells and kinase activity underpinning the bending of developing cochlear duct.

We showed that the mode of luminal-basal nuclear migration switches at a position in the continuous pseudostratified epithelium (Fig. 2D'), which controls the curvature of the MEL (Fig. 2J-M). To our knowledge, we have provided the first experimental evidence that nuclei stall at the luminal side of the pseudostratified epithelium during IKNM in normal development (Norden, 2017). The luminal nuclear stalling results in luminal expansion, to some extent, because of physical space occupation even in the curved pseudostratified epithelium, while it remains unclear whether the luminal nuclear stalling results from the MEL curvature, i.e., the convexity of the luminal side. Therefore, we propose luminal expansion driven by luminal nuclear stalling as a mechanism for sculpting curves in pseudostratified epithelium, in addition to the actomyosin-based basal shrinkage that has been previously reported in zebrafish neuroepithelium (Sidhaye and Norden, 2017; Yanakieva et al., 2019). One important remaining question is what causes the space-dependent mode transition of nuclear movement in the continuous tissue. It has been previously shown that knock-down of cell-surface TAG-1

(transient axonal glycoprotein-1) impedes basalward nuclear movement during IKNM in the mouse ventricular zone, which ultimately leads to overcrowding of neural progenitor cells in the luminal side, and a severe cortical dysplasia(Okamoto et al., 2013). It has been proposed that cytoskeletal machinery, including actomyosin and microtubules, regulates basalward nuclear movement (Kosodo et al., 2011; Norden, 2017; Norden et al., 2009). This provides an important basis for the identification of the molecules responsible for the nuclear behavior in the MEL at the supra-cellular level, which needs to be clarified in the future. In addition, unknown factors providing these molecules with positional information should be explored to understand the mode transition of nuclear movement at the tissue level.

In the present study, the establishment of long-term imaging techniques and biosensors for protein kinase activity has led to the discovery of unexpected spatiotemporal patterns of cell movement and ERK activity in the developing cochlear duct. Previously, we and others have observed intercellular ERK activation waves in the epithelium, such as migrating Madin-Darby canine kidney (MDCK) cells (Aoki et al., 2017; Hino et al., 2020), developing drosophila tracheal placode (Ogura et al., 2018), and wounded murine skin (Hiratsuka et al., 2015). We have also proposed an ERK-mediated mechanochemical feedback system, in which cell extension activates ERK followed by ERK-triggered cell contraction (Boocock et al., 2020; Hino et al., 2020), which can explain the symphony between cell movement and ERK activity.

The ERK activation wave speed in the developing cochlear duct was 0.42 μm min^{-1} (Fig. 4F), which is significantly slower than in MDCK cells and wounded mouse epidermis, where it proceeds at 2.5 μm min^{-1} and 1.4 μm min^{-1}, respectively (Aoki et al., 2017; Hino et al., 2020; Hiratsuka et al., 2015). Interestingly, when normalized to the cell lengths of the developing cochlear duct (4 μm), MDCK cells (20 μm), and the basal cells of the mouse epidermis (10 μm), the wave speed of the developing murine cochlear duct, which is 6 cells hr^{-1}, is comparable with that of MDCK cells, which is 7 cells hr^{-1}, and that of wounded adult murine skin, which is 8 cells hr^{-1}. Our findings couple multicellular flow and ERK activation waves in the cochlea, corroborating the findings of earlier studies (Boocock et al., 2020; Hino et al., 2020), and supporting the existence of a general regulatory mechanism for collective cell migration during tissue morphogenesis.

Our 3D time-lapse imaging revealed coherent helical cell flow from the base-floor to the apex-roof of the lateral side of the cochlear duct. Cell flow analysis revealed that the rate of base-to-apex cell flow (0.24 μm min^{-1}, Fig. S3E) exceeds that of the duct elongation speed (0.13 μm min^{-1}, Mov. 5). Thus, the cell flow rate may be sufficient to compensate for the lateral tissue growth. We speculate that this ERK-mediated cell advection originating from the

409 heterogeneity of cell proliferation causes consistent mediolateral differential growth at the
410 tissue scale, and results in cochlear bending. In support of this, knockout of *Shh* causes a
411 significant decrease in the number of proliferating cells at the base of the cochlear duct, and
412 causes the shortening of the cochlear duct (Bok et al., 2013). As SHH is secreted mainly from
413 the spiral ganglions located in the central axis of the cochlea (Bok et al., 2013), further
414 investigations on the interaction between the cochlear duct and these ganglions will provide a
415 better understanding of cochlear morphogenesis.

416 Overall, we visualized multicellular behavior underlying the bending of the cochlear duct
417 during development using deep tissue live imaging. This contributes to a better understanding
418 of symmetry breaking in tissue morphogenesis during development and in generation of inner
419 ear organoids (Koehler et al., 2017, 2013). The live imaging technique used in the present study
420 forms the basis for further analysis of the interplay between morphogenesis and cell fate
421 decisions during cochlear development (Cohen et al., 2019; Tateya et al., 2019).
422

Acknowledgements

This work was supported by the JSPS KAKENHI 17KT0107 and 19H00993, by the JST PRESTO JPMJPR1949 and CREST JPMJCR1654, and by the Medical Research Support Center of Kyoto University. We would like to thank Akane Kusumi for technical assistance, and Edouard Hannezo, Naoya Hino, and Yoshiko Takahashi for fruitful discussion.

Author contributions

Conceptualization, T.T., T.H.; Methodology, M.I., T.T.. T.H.; Software, M.I., T.H.; Validation, M.I., T.H.; Formal analysis, M.I., T.H.; Investigation, M.I., T.H.; Resources, M.I., M.M., T.H.; Data curation, M.I., T.H.; Writing - original draft, M.I., T.H.; Writing - review & editing, T.T., M.M., T.H.; Visualization, T.H.; Supervision, M.M., T.H.; Project administration, T.H.; Funding acquisition, M.M., T.H.

Competing interests

The authors declare no competing interests.

References

Abe T, Kiyonari H, Shioi G, Inoue KI, Nakao K, Aizawa S, Fujimori T. 2011. Establishment of conditional reporter mouse lines at ROSA26 locus for live cell imaging. *Genesis* **49**:579–590. doi:10.1002/dvg.20753

Aoki K, Kamioka Y, Matsuda M. 2013. Fluorescence resonance energy transfer imaging of cell signaling from in vitro to in vivo: basis of biosensor construction, live imaging, and image processing. *Dev Growth Differ* **55**:515–22. doi:10.1111/dgd.12039

Aoki K, Kondo Y, Naoki H, Hiratsuka T, Itoh RE, Matsuda M. 2017. Propagating Wave of ERK Activation Orients Collective Cell Migration. *Dev Cell* **43**:305-317.e5. doi:10.1016/j.devcel.2017.10.016

Bok J, Zenczak C, Hwang CH, Wu DK. 2013. Auditory ganglion source of Sonic hedgehog regulates timing of cell cycle exit and differentiation of mammalian cochlear hair cells. *Proc Natl Acad Sci U S A*. doi:10.1073/pnas.1222341110

Boocock D, Hino N, Ruzickova N, Hirashima T, Hannezo E. 2020. Theory of mechano-chemical patterning and optimal migration in cell monolayers. *bioRxiv*. doi:https://doi.org/10.1101/2020.05.15.096479

Chen P, Johnson JE, Zoghbi HY, Segil N. 2002. The role of Math1 in inner ear development: Uncoupling the establishment of the sensory primordium from hair cell fate determination. *Development*.

Cohen R, Amir-Zilberstein L, Hersch M, Woland S, Taiber S, Matsuzaki F, Bergmann S, Avraham KB, Sprinzak D. 2019. Shear forces drive precise patterning of hair cells in the mammalian inner ear. *bioRxiv*. doi:10.1101/707422

Driver EC, Northrop A, Kelley MW. 2017. Cell migration, intercalation and growth regulate mammalian cochlear extension. *Dev*. doi:10.1242/dev.151761

Fletcher AG, Osterfield M, Baker RE, Shvartsman SY. 2014. Vertex models of epithelial morphogenesis. *Biophys J* **106**:2291–2304. doi:10.1016/j.bpj.2013.11.4498

Grosse AS, Pressprich MF, Curley LB, Hamilton KL, Margolis B, Hildebrand JD, Gumucio DL. 2011. Cell dynamics in fetal intestinal epithelium: Implications for intestinal growth and morphogenesis. *Development*. doi:10.1242/dev.065789

Groves AK, Fekete DM. 2012. Shaping sound in space: The regulation of inner ear patterning. *Development*. doi:10.1242/dev.067074

Harvey CD, Ehrhardt AG, Cellurale C, Zhong H, Yasuda R, Davis RJ, Svoboda K. 2008. A genetically encoded fluorescent sensor of ERK activity. *Proc Natl Acad Sci U S A*.

474 doi:10.1073/pnas.0804598105
475 Hino N, Rossetti L, Marín-Llauradó A, Aoki K, Trepat X, Matsuda M, Hirashima T. 2020.
476 ERK-mediated mechanochemical waves direct collective cell polarization. *Dev Cell* **in**
477 **press**. doi:10.1101/2019.12.25.888552
478 Hirashima T, Adachi T. 2019. Polarized cellular mechano-response system for maintaining
479 radial size in developing epithelial tubes. *Development* **146**:dev181206.
480 doi:10.1242/dev.181206
481 Hirashima T, Adachi T. 2015. Procedures for the Quantification of Whole-Tissue
482 Immunofluorescence Images Obtained at Single-Cell Resolution during Murine Tubular
483 Organ Development. *PLoS One* **10**:e0135343. doi:10.1371/journal.pone.0135343
484 Hiratsuka T, Fujita Y, Naoki H, Aoki K, Kamioka Y, Matsuda M. 2015. Intercellular
485 propagation of extracellular signal-regulated kinase activation revealed by in vivo
486 imaging of mouse skin. *Elife* **2015**. doi:10.7554/eLife.05178
487 Johnson AB, Fogel NS, Lambert JD. 2019. Growth and morphogenesis of the gastropod
488 shell. *Proc Natl Acad Sci U S A*. doi:10.1073/pnas.1816089116
489 Koehler KR, Mikosz AM, Molosh AI, Patel D, Hashino E. 2013. Generation of inner ear
490 sensory epithelia from pluripotent stem cells in 3D culture. *Nature*.
491 doi:10.1038/nature12298
492 Koehler KR, Nie J, Longworth-Mills E, Liu XP, Lee J, Holt JR, Hashino E. 2017. Generation
493 of inner ear organoids containing functional hair cells from human pluripotent stem
494 cells. *Nat Biotechnol*. doi:10.1038/nbt.3840
495 Komatsu N, Aoki K, Yamada M, Yukinaga H, Fujita Y, Kamioka Y, Matsuda M. 2011.
496 Development of an optimized backbone of FRET biosensors for kinases and GTPases.
497 *Mol Biol Cell* **22**:4647–56. doi:10.1091/mbc.E11-01-0072
498 Komatsu N, Terai K, Imanishi A, Kamioka Y, Sumiyama K, Jin T, Okada Y, Nagai T,
499 Matsuda M. 2018. A platform of BRET-FRET hybrid biosensors for optogenetics,
500 chemical screening, and in vivo imaging. *Sci Rep*. doi:10.1038/s41598-018-27174-x
501 Kosodo Y, Suetsugu T, Suda M, Mimori-Kiyosue Y, Toida K, Baba SA, Kimura A,
502 Matsuzaki F. 2011. Regulation of interkinetic nuclear migration by cell cycle-coupled
503 active and passive mechanisms in the developing brain. *EMBO J*.
504 doi:10.1038/emboj.2011.81
505 Liu Z, Owen T, Zhang L, Zuo J. 2010. Dynamic expression pattern of sonic hedgehog in
506 developing cochlear spiral ganglion neurons. *Dev Dyn*. doi:10.1002/dvdy.22302
507 Mao Y, Mulvaney J, Zakaria S, Yu T, Morgan KM, Allen S, Basson MA, Francis-West P,

Irvine KD. 2011. Characterization of a Dchs1 mutant mouse reveals requirements for Dchs1-Fat4 signaling during mammalian development. *Development*. doi:10.1242/dev.057166

Mao Y, Tournier AL, Hoppe A, Kester L, Thompson BJ, Tapon N. 2013. Differential proliferation rates generate patterns of mechanical tension that orient tissue growth. *EMBO J* **32**:2790–2803. doi:10.1038/emboj.2013.197

Meyer EJ, Ikmi A, Gibson MC. 2011. Interkinetic nuclear migration is a broadly conserved feature of cell division in pseudostratified epithelia. *Curr Biol*. doi:10.1016/j.cub.2011.02.002

Montcouquiol M, Kelley MW. 2020. Development and patterning of the cochlea: From convergent extension to planar polarity. *Cold Spring Harb Perspect Med*. doi:10.1101/cshperspect.a033266

Nagai T, Honda H. 2001. A dynamic cell model for the formation of epithelial tissues. *Philos Mag Part B* **81**:699–719. doi:10.1080/13642810108205772

Norden C. 2017. Pseudostratified epithelia - cell biology, diversity and roles in organ formation at a glance. *J Cell Sci*. doi:10.1242/jcs.192997

Norden C, Young S, Link BA, Harris WA. 2009. Actomyosin Is the Main Driver of Interkinetic Nuclear Migration in the Retina. *Cell*. doi:10.1016/j.cell.2009.06.032

Ogura Y, Wen F-L, Sami MM, Shibata T, Hayashi S. 2018. A Switch-like Activation Relay of EGFR-ERK Signaling Regulates a Wave of Cellular Contractility for Epithelial Invagination. *Dev Cell* **46**:162-172.e5. doi:10.1016/j.devcel.2018.06.004

Okamoto M, Namba T, Shinoda T, Kondo T, Watanabe T, Inoue Y, Takeuchi K, Enomoto Y, Ota K, Oda K, Wada Y, Sagou K, Saito K, Sakakibara A, Kawaguchi A, Nakajima K, Adachi T, Fujimori T, Ueda M, Hayashi S, Kaibuchi K, Miyata T. 2013. TAG-1-assisted progenitor elongation streamlines nuclear migration to optimize subapical crowding. *Nat Neurosci*. doi:10.1038/nn.3525

Okuda S, Inoue Y, Eiraku M, Adachi T, Sasai Y. 2014. Vertex dynamics simulations of viscosity-dependent deformation during tissue morphogenesis. *Biomech Model Mechanobiol* **14**:413–425. doi:10.1007/s10237-014-0613-5

Pauley S, Wright TJ, Pirvola U, Ornitz D, Beisel K, Fritzsch B. 2003. Expression and function of FGF10 in mammalian inner ear development. *Dev Dyn*. doi:10.1002/dvdy.10297

Pirvola U, Spencer-Dene B, Xing-Qun L, Kettunen P, Thesleff I, Fritzsch B, Dickson C, Ylikoski J. 2000. FGF/FGFR-2(IIIb) Signaling Is Essential for Inner Ear

542 Morphogenesis. *J Neurosci* **20**:6125–6134. doi:10.1523/JNEUROSCI.20-16-
543 06125.2000
544 Qian D, Jones C, Rzadzinska A, Mark S, Zhang X, Steel KP, Dai X, Chen P. 2007. Wnt5a
545 functions in planar cell polarity regulation in mice. *Dev Biol*.
546 doi:10.1016/j.ydbio.2007.03.011
547 Raup DM, Michelson A. 1965. Theoretical morphology of the coiled shell. *Science (80-)*.
548 doi:10.1126/science.147.3663.1294
549 Riedl J, Flynn KC, Raducanu A, Gärtner F, Beck G, Bösl M, Bradke F, Massberg S, Aszodi
550 A, Sixt M, Wedlich-Söldner R. 2010. Lifeact mice for studying F-actin dynamics. *Nat*
551 *Methods*. doi:10.1038/nmeth0310-168
552 Saburi S, Hester I, Fischer E, Pontoglio M, Eremina V, Gessler M, Quaggin SE, Harrison R,
553 Mount R, McNeill H. 2008. Loss of Fat4 disrupts PCP signaling and oriented cell
554 division and leads to cystic kidney disease. *Nat Genet*. doi:10.1038/ng.179
555 Saffer AM, Carpita NC, Irish VF. 2017. Rhamnose-Containing Cell Wall Polymers Suppress
556 Helical Plant Growth Independently of Microtubule Orientation. *Curr Biol*.
557 doi:10.1016/j.cub.2017.06.032
558 Sauer FC. 1935. Mitosis in the neural tube. *J Comp Neurol* **62**:377–405.
559 doi:10.1002/cne.900620207
560 Serra-Picamal X, Conte V, Vincent R, Anon E, Tambe DT, Bazellieres E, Butler JP,
561 Fredberg JJ, Trepat X. 2012. Mechanical waves during tissue expansion. *Nat Phys*
562 **8**:628–634. doi:10.1038/nphys2355
563 Sidhaye J, Norden C. 2017. Concerted action of neuroepithelial basal shrinkage and active
564 epithelial migration ensures efficient optic cup morphogenesis. *Elife*.
565 doi:10.7554/eLife.22689
566 Smyth DR. 2016. Helical growth in plant organs: Mechanisms and significance. *Dev*.
567 doi:10.1242/dev.134064
568 Tateya T, Imayoshi I, Tateya I, Hamaguchi K, Torii H, Ito J, Kageyama R. 2013. Hedgehog
569 signaling regulates prosensory cell properties during the basal-to-apical wave of hair cell
570 differentiation in the mammalian cochlea. *Dev*. doi:10.1242/dev.095398
571 Tateya T, Sakamoto S, Ishidate F, Hirashima T, Imayoshi I, Kageyama R. 2019. Three-
572 dimensional live imaging of Atoh1 reveals the dynamics of hair cell induction and
573 organization in the developing cochlea. *Dev*. doi:10.1242/dev.177881
574 Thompson DW. 1942. On Growth and Form, Revised ed. ed, On growth and form. Dover
575 Publications. doi:10.2307/2019330

576 Urness LD, Wang X, Doan H, Shumway N, Noyes CA, Gutierrez-Magana E, Lu R, Mansour
577 SL. 2018. Spatial and temporal inhibition of FGFR2b ligands reveals continuous
578 requirements and novel targets in mouse inner ear morphogenesis. *Dev*.
579 doi:10.1242/dev.170142
580 Urness LD, Wang X, Shibata S, Ohyama T, Mansour SL. 2015. Fgf10 is required for
581 specification of non-sensory regions of the cochlear epithelium. *Dev Biol*.
582 doi:10.1016/j.ydbio.2015.01.015
583 Wada H, Matsumoto D. 2018. Twisting Growth in Plant Roots In: Gitmann A, Grill J,
584 editors. Plant Biomechanics; From Structure to Function at Multiple Scales. Springer
585 International Publishing. pp. pp127-140.
586 Wang J, Mark S, Zhang X, Qian D, Yoo SJ, Radde-Gallwitz K, Zhang Y, Lin X, Collazo A,
587 Wynshaw-Boris A, Chen P. 2005. Regulation of polarized extension and planar cell
588 polarity in the cochlea by the vertebrate PCP pathway. *Nat Genet*. doi:10.1038/ng1622
589 Yamamoto N, Okano T, Ma X, Adelstein RS, Kelley MW. 2009. Myosin II regulates
590 extension, growth and patterning in the mammalian cochlear duct. *Development*.
591 doi:10.1242/dev.030718
592 Yanakieva I, Erzberger A, Matejčić M, Modes CD, Norden C. 2019. Cell and tissue
593 morphology determine actin-dependent nuclear migration mechanisms in neuroepithelia.
594 *J Cell Biol*. doi:10.1083/jcb.201901077
595
596

Materials and Methods

(1) Experiments

Animals

For FRET imaging, we used the transgenic mice that ubiquitously express an ERK biosensor with a long flexible linker (hyBRET-ERK-NLS) reported elsewhere(Harvey et al., 2008; Komatsu et al., 2018, 2011) . For simultaneous imaging of F-actin and nuclei, we crossed Lifeact-EGFP (Riedl et al., 2010) and R26-H2B-mCherry(Abe et al., 2011). Lifeact-EGFP mice were generously provided by Takashi Hiiragi from EMBL Heidelberg and R26-H2B-mCherry mice were provided from RIKEN Large (CDB0204K). Otherwise, we used ICR mice purchased from Japan SLC, Inc. We designated the midnight preceding the plug as embryonic day 0.0 (E0.0), and all mice were sacrificed by cervical dislocation to minimize suffering. All the animal experiments were approved by the local ethical committee for animal experimentation (MedKyo 19090 and 20081) and were performed in compliance with the guide for the care and use of laboratory animals at Kyoto University.

Antibodies

The following primary and secondary antibodies were used for immunofluorescence: anti-E-cadherin rat antibody (Cell Signaling Technology, #3195, 1:100 dilution), anti-Myosin-VIIa rabbit polyclonal antibody (Proteus BioSciences Inc., #25-6790, 1:200 dilution), anti-Histone H3 (phospho S28) rat polyclonal antibody (Abcam, #ab10543, 1:200 dilution), Alexa Fluor 546-conjugated goat anti-rat IgG (H+L) antibody (Thermo Fisher Scientific, #A11081, 1:1000 dilution), Alexa Fluor 647-conjugated goat anti-rabbit IgG (H+L) antibody (Abcam, #ab150079, or Thermo Fisher Scientific, #A21247, 1:1000 dilution).

Small-molecule inhibitors

The following chemicals were used: Mitomycin C (Nacalai Tesque, #20898-21) and PD0325901 (FUJIFILM Wako Pure Chemical Corporation, #162-25291).

Whole-tissue staining and imaging

The cochleae were gently freed from the capsule and the staining and clearing were performed according to an earlier study (Hirashima and Adachi, 2015). Briefly, the samples were fixed with 4% PFA in PBS overnight at 4°C and then blocked by incubation in 10% normal goat serum (Abcam, #ab156046) diluted in 0.1% Triton X-100/PBS (PBT) for 3 h at 37°C. The

631 samples were treated with primary antibodies overnight at 4°C, washed in 0.1% PBT, and
632 subsequently treated with secondary antibodies conjugated to either Alexa Fluor 546 or Alexa
633 Fluor 647 overnight at 4°C. For counter staining of nucleus, we mixed Hoechst 33342 (5 µg/ml,
634 Dojindo Molecular Technologies, #H342-10) or DAPI (Dojindo Molecular Technologies,
635 #D523-10, 1:200 dilution) . The samples were mounted with 10 µL of 1% agarose gel onto a
636 glass-based dish (Greiner Bio-One, #627871) for stable imaging. Then, the samples were
637 immersed with the BABB (benzyl-alcohol and benzyl-benzoate, 1:2, #04520-96 and # 04601-
638 65, Nacalai Tesque) solution or CUBIC-R+ (Tokyo Chemical Industry Co., # T3741) solution
639 for optical clearing. Images were acquired using the confocal laser scanning platform Leica
640 TCS SP8 equipped with the hybrid detector Leica HyD with the ×40 objective lens (NA = 1.3,
641 WD = 240 µm, HC PL APO CS2, Leica) and the Olympus FluoView FV1000 with the ×30
642 objective lens (NA = 1.05, WD = 0.8 mm, UPLSAPO30XS, Olympus).
643
644 **EdU assay**
645 For EdU incorporation to embryos, 200 µL of 5 mg/mL EdU in PBS was intraperitoneally
646 injected to pregnant mice 30 min prior to dissection. For the incorporation to dissected cochleae,
647 10 µM of EdU was treated into the samples 1 hour prior to the chemical fixation. Before EdU
648 detection, whole-tissue immunofluorescence of E-cadherin and counter nuclei staining with
649 DAPI were performed. EdU was detected using the Click-iT® EdU Imaging Kits (Thermo
650 Fisher Scientific, #C10340). The samples were optically cleared with CUBIC-R+ and images
651 were acquired by confocal microscopy as described above.
652
653 **Mosaic cell labeling**
654 DNA solutions of the pCAG-GFP vectors (0.7 µg/µL) in PBS with 0.1% Fast Green FCF
655 (Sigma-Aldrich, #F7252-5G) were injected into the lumen of an inner ear dissected from E13.5
656 embryos through a fine glass capillary tube under a stereo microscope (SZ61, Olympus). After
657 injection of DNA solution, the cochlea was sandwiched by a pair of tweezer type electrodes
658 (Nepa Gene Co., #CUY650P5) and the DNA was electrotransferred using the NEPA21 Super
659 Electroporator (Nepa Gene Co.). Three 5 msec square pulses (175 V, +) with a 10% decay rate
660 at intervals of 50 msec were applied as poring pulses, followed by three 50 msec square pulses
661 (10 V, +/–) with a 40% decay rate at intervals of 50 msec as transfer pulses.
662
663 **Surgical separation**
664 We dissected cochleae from embryos at E17.5 and manually separated a cochlear duct into the

665 medial and lateral side. The images in Movie 3 were acquired using the stereomicroscope
666 (SZX16, Olympus) with a cooled color CCD camera (DP73, Olympus).
667
668 **Explant cultures**
669 We cultured the dissected cochleae without removing the capsule otherwise noted. The
670 cochleae were mounted on a the 35 mm glass based dish (Iwaki, #3910-035) with 1 μL of
671 growth factor reduced Matrigel (Corning, #356231), and filled with 2 mL of a culture medium
672 including FluoroBrite DMEM Media (Thermo Fischer Scientific, #A1896701) with 1%
673 GlutaMAX (Thermo Fischer Scientific, #35050061) and 1% N2 Supplement with Transferrin
674 (Holo)(FUJIFILM Wako Pure Chemical Corporation, #141-08941). The samples were
675 incubated at 37°C under 5% CO_2.
676
677 **Live imaging for explants**
678 We used two different sample preparations for live imaging under ex vivo culture condition.
679 For imaging of MEL, we completely removed the capsule and put the uncovered cochlear duct
680 attached with spiral ganglion onto the glass-bottom dish whose apex side faces the glass. For
681 long-term organ-scale imaging, we partially cut off the capsule adjacent to the apex tip of
682 cochlear duct using tweezers carefully, and the semicircular canals were removed. The isolated
683 cochlea was put onto the dish as described above. The former method allows us to take images
684 MEL at single cell resolution but failed to achieve elongation and bending of cochlear duct. In
685 contrast, the latter method recapitulates the cochlear duct morphogenesis but was unable to
686 detect fluorescence signals in the medial side. For microscopy, we used an incubator-integrated
687 multiphoton fluorescence microscope system (LCV-MPE, Olympus) with a ×25 water-
688 immersion lens (NA=1.05, WD=2 mm, XLPLN25XWMP2, Olympus) and an inverted
689 microscope (FV1200MPE-IX83, Olympus) with a ×30 silicone-immersion lens (NA=1.05,
690 WD=0.8 mm, UPLSAPO30XS, Olympus). The excitation wavelengths were set to 840 nm,
691 930 nm, and 1040 nm each for CFP, Lifeact-EGFP, and R26-H2B-mCherry (InSight DeepSee,
692 Spectra-Physics). Imaging conditions for Lifeact-EGFP and R26-H2B-mCherry were as
693 follows – scan size: 800×800 pixels, scan speed: 4.0 μsec/pixel, IR cut filter: RDM690
694 (Olympus), dichroic mirrors: DM505 and DM570 (Olympus), and emission filters: BA495-
695 540 for EGFP and BA575-630 for mCherry (Olympus). Imaging conditions for the FRET
696 biosensor were as follows – scan size: 800 × 800 pixels, scan speed: 10 μsec/pixel, IR cut filter:
697 RDM690 (Olympus), dichroic mirrors: DM505 and DM570 (Olympus), and emission filters:
698 BA460-500 for CFP and BA520-560 for FRET detection (Olympus).

699

700 **(2) Quantification and Analysis**

701

702 **FRET image analysis**

703 Image processing for FRET measurement was described elsewhere (Aoki et al., 2013). Briefly,
704 the median filter of 3×3 window was processed to remove shot noises, and background signal
705 was subtracted each in FRET channel and CFP channel. Then, the ratio of FRET intensity to
706 the CFP intensity was calculated by a custom-made MATLAB (MathWorks) script.

707

708 **Measurement of layer curvature and thickness**

709 For 2D measurement of curvature and thickness, we first performed whole-mount
710 immunofluorescence of E-cadherin to visualize the cochlear epithelium and acquired z-stack
711 images by confocal microscopy as described above. Next, we manually traced the apical and
712 basal side of epithelial cells on the middle horizontal section of the roof-floor axis. The
713 extracted epithelial layer was named as the medial/lateral epithelial layer according to the side
714 based on a given apex tip point. Then, the curve of the epithelial layer was obtained by the
715 iterative skeletonization, and discrete points (x_i, y_i) were sampled along the curves at regular
716 intervals of 15 μm. Finally, fitting the discrete points with a cubic spline function, the function
717 S_i at an interval $[x_i, x_{i+1}]$ is denoted as

718

719 $$S_i(x) = a_i(x - x_i)^3 + b_i(x - x_i)^2 + c_i(x - x_i) + d_i.$$

720

721 Due to a definition of curvature $\kappa(x) = S''(1 + S'^2)^{-3/2}$, the curvature from the spline
722 function was calculated as

723

724 $$\kappa_i(x) = \frac{6a(x - x_i) + 2b}{(1 + \{3a(x - x_i)^2 + 2b(x - x_i) + c\}^2)^{3/2}}.$$

725

726 The curve of the convex/concave to the duct lumen was assigned as positive/negative in κ. We
727 defined the layer thickness as a linear length connecting to the luminal and basal edge, which
728 is vertical to the curve of the epithelial layer at sampling points.

729

730 **Quantification of nuclear migration**

731 We manually measured the center position of a daughter cell and its luminal and basal edge.

Based on the cross point where the luminal-basal line and center line of medial epithelial layer are intersected, we calculated the arc length from the duct tip to the nuclear position using a custom built MATLAB code.

Angle measurement of cell division orientation

First, we performed two-photon live imaging using FV1200MPE-IX83 as described above, and obtained volumetric images with a depth interval of 3 μm. In each mitotic event, we then manually measured position (x, y, z) of the two daughter cells 3 hours later after the mitosis in the fixed coordinate system O of the 3D image. Also, we manually acquired the position of the luminal and basal edge of the mother cell to define a position (x', y', z') in a local coordinate system, O′, the origin of which is the middle point of the two daughter nuclei. Each orthogonal basis of the O′ coordinate was defined as follows: the apex-base axis in the MEL (x′), the surface normal of the MEL (y′), i.e., luminal-basal axis in the MEL, and roof-floor axis (z′) orthogonal to both x′ and y′ according to the right-handed system. With this local coordinate system, we finally calculated two angles φ and θ in the local sphere coordinate resulting from coordinate transformation from the O into the O′ system.

EdU intensity mapping

First, we separated 8-bit image stacks into two, roof and floor, based on z position at the middle point, and performed maximum intensity projection onto xy plane both for staining images for E-cadherin and EdU. Next, we binarized immunostaining signals for E-cadherin using Otsu's method with morphological operations and detected periphery of the cochlear duct with the MATLAB function 'bwperim'. With three reference points given manually, i.e., a) the duct tip, b) the end point of MEL and c) that of LEL, the MEL and LEL curve was each defined by connecting points between a) and b) and those between a) and c) along the duct periphery. Then, we marked points to make 20 bins at a constant distance each along the MEL curve and LEL curve. By connecting the marked point of MEL and that of LEL indexed by an order from the duct tip and dividing the lines into 10, we partitioned the cochlear duct into small regions for the measurement. Finally, we measured the averaged intensity of EdU signal within each region and normalized by 255.

Tissue flow and ERK activity

To calculate velocity fields of cells in cochleae, we performed particle image velocimetry (PIV)-based image processing using a free code MatPIV (a GNU public license software

distributed by Prof. Kristian Sveen in University of Oslo) was applied to time-lapse images of the CFP channel. Velocity fields at time T was computed by displacement between T and $T+\Delta t$. Δt was set as the sampling rate, 12 min. The size of the interrogation window was set to 40 pixels, approximately 25 μm, corresponding to 4-5 cell diameter, and the window overlap was set to 50%. The obtained velocity data were then smoothened via median filtering to eliminate peaky noises. We then obtained the 'tissue flow speed for the elongation' from PIV velocity vector projected onto the apex-base line depicted in Figure 4D, and calculated the spatial derivative of the tissue flow speed for the elongation between two adjacent interrogation windows on the apex-base line according to the definition of a diagonal component of the strain rate. This quantity was smoothened using the MATLAB function 'smooth' to eliminate high frequency components and defined as the extension-shrinkage rate. As for the ERK activity, we set thresholds in CFP images using Otsu's method within each interrogation window to extract cytoplasmic region and calculated the mean FRET/CFP ratio in the binarized region. The ERK activity rate was calculated as the time derivative of the ERK activity. Cross-correlation analysis was performed using the MATLAB function 'xcorr'.

Statistical analysis

The number of cells or region of interests analyzed (n) and the number of biological replicates (N) are indicated in the figure legends. No particular statistical method was used to predetermine the sample size. A minimum of N=3 independent experiments were performed based on previous studies in the field. No inclusion/exclusion criteria were used and all analyzed samples were included in the analysis. No randomization was performed. Statistical tests, sample sizes, test statistics, and P-values were described in the main text. P-values of less than 0.05 were considered to be statistically significant in two-tailed tests, and were classified as 4 categories; * (P<0.05), ** (P<0.01), *** (P<0.001), and n.s. (not significant, i.e., $P \geq 0.05$).

Software

For digital image processing, we used MATLAB (MathWorks) and Image J (National Institute of Health). For graphics, we used MATLAB (MathWorks), Imaris (Bitplane) and ImageJ (National Institute of Health). For statistical analysis, we used MATLAB (MathWorks).

(3) Mathematical model

A-1. A mechanical model for MEL morphogenesis

We modeled multicellular dynamics within an epithelial layer using a vertex dynamics model (VDM) (Fletcher et al., 2014; Hirashima and Adachi, 2019; Nagai and Honda, 2001). Here we focused on two-dimensional section on apex-base and roof-floor axes as shown in Fig. 2A. In general, the 2D VDM model represents a single cell as a polygon, of which vertices are elementary points that constitute the cell shape, and a group of cells is regarded as a set of polygons shared by neighboring cells – we put four vertices, two of which are regarded as an luminal edge and the other two of which are as a basal edge.

In the VDM, the dynamics of position of vertex i, r_i, obey the equation of motion based on the principle of least potential energy U as follows:

$$\eta(\dot{r}_i - v_i) = -\nabla_i U, \qquad \text{Eq. 1}$$

where η is a viscosity coefficient. v_i is a local velocity of vertex i, defined as $\langle v_i \rangle = \langle \dot{r}_{j_i} \rangle_{j_i}$, where j_i is an index of cells contacting to vertex i, r_{j_i} is a centroid of cell j_i, and $\langle\ \rangle_{j_i}$ denotes averaging in j_i (Hirashima and Adachi, 2019; Mao et al., 2013; Okuda et al., 2014). For a potential energy as a minimum expression, we defined as

$$U = \sum_j \left\{ \frac{k_a}{2}\left(a_j - a_j^*\right)^2 + \frac{k_b}{2}\left(b_j - b_j^*\right)^2 + \frac{k_l}{2}\left(l_j - l_j^*\right)^2 + \frac{k_A}{2}\left(A_j - A_j^*\right)^2 \right\} + \sum_i \frac{k_\theta}{2}{\theta_i}^2. \qquad \text{Eq. 2}$$

The first to third terms each represent a regulation of cell edge length in luminal/apical, basal, and lateral side with controlling parameters (k_a, k_b, k_l), current length (a_j, b_j, l_j), and the target length (a_j^*, b_j^*, l_j^*). Target edge length of the luminal/apical and that of basal side are a function of nuclear position within the epithelial layer, described later. The fourth term represents cell area preservation with its coefficient k_A, current cell area A_j, and the target cell area A_j^*. The fifth term represents bending energy of the luminal/apical side and that of basal side attributed to each vertex; k_θ denotes the bending rigidity and θ_i is an angle of luminal/apical edge or that of basal edge at a vertex i. Although the cell shape is relatively flexible in a pseudostratified epithelial tissue, this model framework is valid as several biological features can be incorporated, such as the nuclear position-dependent edge regulation and cell size preservation.

Each cell has a unique cell cycle, length of which τ_{div} is assumed to be equally assigned to all cells. We assume that a period of each cell cycle phase (G1, S, G2, and M) is partitioned

as 11:8:4:1, and a cell cycle status or timer τ_j, origin of which is defined at the end of cell division, i.e., a boundary of M-G1, is provided according to the distribution of cell cycle phase. We model that the cell timer τ_j in the cycle determines the distance from the luminal side of a cell, i.e., nuclear position d_j $(0 \leq d_j \leq 1)$, with a parameter γ as follows:

$$d_j = \begin{cases} 2\gamma\tau_j/\tau_{div} & (0 < \tau_j \leq 0.5\tau_{div}) \\ (-\tau_j/\tau_{div} + 0.95)\gamma/0.45 & (0.5\tau_{div} < \tau_j \leq 0.95\tau_{div}) \\ 0 & (0.95\tau_{div} < \tau_j \leq \tau_{div}). \end{cases} \quad \text{Eq. 3}$$

This means that nuclei move toward the basal side of cell during G1-S phase with a degree γ and get close to the luminal side before entering M phase. Of note, γ controls the degree of basalward movement as described in the main text. Once a cell divides, τ_j in one of daughter cells reset to zero and one in the other is set to a value stochastically chosen from 0 to $0.1\tau_{div}$ with a uniform distribution to avoid perfect synchronization between neighboring cells.

Occupied cell area is dominant in the medial epithelial layer and the cell position along the luminal-basal axis should regulate the length of luminal edge and that of basal edge. Thus, we define the target length as the simplest linear function of the nuclear position with two parameters ξ_{max} and ξ_{min} as follows:

$$a_j^* = (\xi_{min} - \xi_{max})d_j + \xi_{max},$$
$$b_j^* = (\xi_{max} - \xi_{min})d_j + \xi_{min}. \quad \text{Eq. 4}$$

A-2. Numerical simulation

The ordinary differential equations were numerically solved by the forward Euler method with time step 0.01. The code was generated with MATLAB (MathWorks). Regarding initial condition, 20 rectangular cells, width/height of each which is 2.5/50 μm, are arrayed along a horizontal line. Standard parameter set is $\eta = 1$, $k_A = 0.01$, $a_j^* = 125\ [\mu m^2]$, $k_a = 1$, $k_b = 1$, $k_l = 1$, $k_\theta = 30$, $l_j^* = 50\ [\mu m]$, $\tau_{div} = 432$, $\gamma = 0.9$, $\xi_{max} = 5\ [\mu m]$, $\xi_{min} = 1\ [\mu m]$, otherwise noted. a_j^*, l_j^*, γ, ξ_{max}, and ξ_{min} were determined from obtained images, and other parameters were determined empirically with some observations; at first, η, k_a, k_b, and k_l were set to 1 and then k_A, τ_{div}, and k_θ were determined to reproduce the MEL curvature observed in the curvature experimentally. Note that relative values rather than

absolute ones are critical for the dynamics.

A-3. Detailed setting in virtual experiments for cell cycle arrest

For an investigation towards mimicking the developmental process, we introduced luminal stalling region, defined with an arclength along the epithelial layer L originated from the boundary of apex side. Assuming once the cells in the luminal stalling region undergo division, the daughter cells' timer τ_j do not count up, meaning that those nuclei stay at the luminal side without reentering the cell cycle. This is due to experimental observations in which daughter cells do not undergo mitosis exclusively in the curved region within a short time scale, at least our observation window. For the cells in the non-luminal stalling region, τ_{div} was set stochastically chosen from a uniform distribution from 216 to 864 each after the cell division to incorporate variability and asynchronicity in nuclear dynamics. To recapitulate the mitomycin C treatment in simulation, the cell cycle was arrested if the cell timer τ_j was ranged in $0.25\tau_{div}$ to $0.8\tau_{div}$, corresponding to the mid G1 phase to the end of S phase, when the simulation time exceeded 700. For the control case, we evaluated the curvature of virtual MEL when the cell number reached at 100. For the case of mitomycin C treatment, we evaluated when the simulation time reached at 1300 because the averaged simulation time in the control case was 1298 (n=10).

B-1. Modeling oscillatory ERK activation waves and cell flows

We built a minimal 1D mechano-chemical coupling model for the collective cell migration based on our previous studies (Boocock et al., 2020; Hino et al., 2020). Cells, each indexed as j=1,...,N, are represented as a chain of springs, whose junctions including the boundaries are labeled as i=1,...,N+1, with elastic constant k and each cell generates contractile force at the rear side of the cell to move to the front with a force F. *i.e.*, the cell contractile force with $j=N$ ($F_{j=N}$) is regarded as the force at the junction $i=N$ ($F_{i=N}$). Because the epithelial cells adhere to neighboring cells and thus transmit the elastic force with viscous frictions $\boldsymbol{\eta_c}$, the dynamics of cell collectives is represented as

$$\boldsymbol{\eta_c \dot{x}_i = k(\varepsilon_j - \varepsilon_{j+1}) + F_{j=i}},$$
$$\boldsymbol{\varepsilon_j = (x_{i+1} - x_i)/L - 1}, \qquad \text{for } i = 1,...,N \quad \text{and} \quad j = 1,...,N \qquad \text{Eq. 5}$$

where $\boldsymbol{\varepsilon}$ is a cell strain and L is a typical cell length, i.e., 5 μm. At the front edge of the cells, *i.e.*, $i=N+1$, a self-propelling force F_{tip} is generated, reflecting an elongation of the duct tip. Since the cells respond to stretching as activating the ERK, a coupling between the cell kinematics and the ERK activity is formulated as

$$\boldsymbol{\eta_E \dot{E}_j = \tanh(\alpha \varepsilon_j) - E_j}, \qquad \text{Eq. 6}$$

where α denotes a sensitivity parameter and $\boldsymbol{\eta_E}$ denotes a timescale of the dynamics. Then, the ERK activity is converted to the self-contractile force represented as dynamics of the

$$\boldsymbol{\eta_F \dot{F}_j = \lambda E_j - F_j}, \qquad \text{Eq. 7}$$

where $\boldsymbol{\lambda}$ denotes a controlling parameter of amplitude, and $\boldsymbol{\eta_F}$ denotes a timescale.

As for the uncoupling regime, ERK activity was given as the following traveling waves instead of Eq. 6:

$$\boldsymbol{E(X) = \left(\sin\left(\frac{\pi X}{w} + vt\right) + 1\right) \times 0.5}, \qquad \text{Eq. 8}$$

where w is the characteristic length of ERK activation and v is the ERK activation speed. The parameters w was set as 84 μm, i.e., the wavelength of the ERK activity is 168 μm, from Figure 4E and v was set as 0.42 μm min^{-1} from Figure 4F.

B-2. Numerical simulation

The ordinary differential equations were numerically solved by the forward Euler method with time step 0.01 using the MATLAB. The number of cells N was set as 1000 and the one boundary $i=1$ was fixed and the other $i=N+1$ was the moving boundary condition. Biologically plausible parameter set was determined as $\boldsymbol{\eta_c}$ = 40 [nN min μm^{-1}], $\boldsymbol{k}$ = 20 [nN], F_{tip} = 6 [nN], $\boldsymbol{\alpha}$ = 3, $\boldsymbol{\eta_E}$ = 30 [min], $\boldsymbol{\eta_F}$ = 10 [min], and $\boldsymbol{\lambda}$ = 9 [nN] according to the present study and a previous study (Serra-Picamal et al., 2012).

Supplementary figure legends

Figure S1 Morphological quantification of epithelial layer

Curvature and thickness as a function of the arc length from the tip along the lateral epithelial layer (LEL, left) and the medial epithelial layer (MEL, right) at E13.5 to E15.5. Mean ± s.d. N=3.

Figure S2 Luminal-basal nuclear movement in the MEL

(A) Numerical investigation of the mathematical model. The curvature is plotted over $\boldsymbol{\gamma}$. Mean ± s.d. N=10. (B) Treatment of cochlea with 10 μM mitomycin C for 1 day. Maximum intensity projection of immunostained images for the anti-E-cadherin (white) and EdU labelling (magenta). Scale bar, 100 μm.

Figure S3 ERK activity waves and cell flows

(A) Roof plane (orange dotted line) in the cross section view of 3D ERK activity map in the cochlea at E12.5. Scale bar, 50 μm. (B) Time-lapse snapshots of ERK activity map in the roof plane. Time indicates the elapsed time of live imaging. Scale bar, 100 μm. (C) Time-lapse snapshots of tissue flow speed obtained by the PIV in the roof plane. The multicellular flows direct toward the elongation direction around the duct tip despite winding in the region away from the tip in the roof side. Scale bar, 100 μm. (D) Kymograph of ERK activity for the two samples. Horizontal axis indicates the position on the apex-base line and vertical axis indicates the elapsed time of live imaging. Dotted lines represent the oscillatory wave trains from the apex to the base. Scale bar, 100 μm. (E) Time-series data of ERK activity and the tissue flow speed for elongation in the three different ROIs. (F) ERK activity before and after the MEK inhibitor PD0325901 treatment at 1 μM. Scale bar, 20 μm.

Figure S4 Mathematical model for ERK activation waves and cell flows

(A, A') Schematics for two regimes. ERK activity and cell deformation is reciprocally regulated in the mechano-chemical coupling regimes (A), but is unidirectionally regulated from the ERK activity to the cell deformation without closed feedbacks in the uncoupling regime (A'). (B, B') Kymograph of the ERK activity. In the mechano-chemical coupling regime, the ERK activity propagation from the apex to the base can be generated (B), even without given ERK wave as shown in the uncoupling regime (B'). Scale bar, 100 μm. (C, C') Time-series of ERK activity rate and extension-shrinkage rate in the coupling (C) and the uncoupling regime (C'). (D, D')

964 Cross-correlation between the extension-shrinkage rate and the ERK activity rate in the
965 coupling (D) and the uncoupling regime (D'). The lag time in (D) is -28 min, compatible with
966 the experiments, while the lag time in (D') is -2 min, almost no lag time.
967
968
969
970

971 **Movie legends**

972 **Movie S1 Real-time movie showing surgical separation of the cochlear duct at E17.5,**
973 **related to Figure 1.**
974 After separation, the medial and lateral tissue are placed on the left and the right, respectively.
975 Note that the medial tissue remains curled even after being straightened.
976
977 **Movie S2 Time-lapse movie of MEL in the cochlear duct at E14.5, related to Figure 2.**
978 Representative nuclei are labelled when those reach at the luminal surface. Green and magenta
979 each denote the nucleus in the flat region and in the curved region. Time interval is 5 min.
980
981 **Movie S3 Model simulation for cell cycle arrest, related to Figure 2.**
982 Color in the epithelial layer indicates the curvature and that in the circles indicate the cell cycle
983 state. Interkinetic nuclear migration is stopped at a timing of cell cycle arrest shown in the right
984 panel.
985
986 **Movie S4 3D ERK activity map of the cochlear at E12.5, related to Figure 4.**
987 Color indicates the ERK activity level shown in Figure 4A. Views from roof side at initial, and
988 ones from apex side at last.
989
990 **Movie S5 Time-lapse movie of the ERK activity and multicellular tissue flow, related to**
991 **Figure 4.**
992 Color in the left panel indicates the ERK activity level shown in Figure 4B and that in the right
993 panel indicates the PIV speed shown in Figure 4C. Views at the floor plane indicated in Figure
994 4A'. Time intervals is 12 min.
995
996 **Movie S6 3D time-lapse imaging of ERK activity in the lateral side of the cochlear duct**
997 **at E12.5, related to Figure 4.**
998 Color indicate the ERK activity level shown in Figure 4J. Views from the lower left corner of
999 Figure 4B. Green arrow indicates the ERK activation peak.
1000

Figure 1

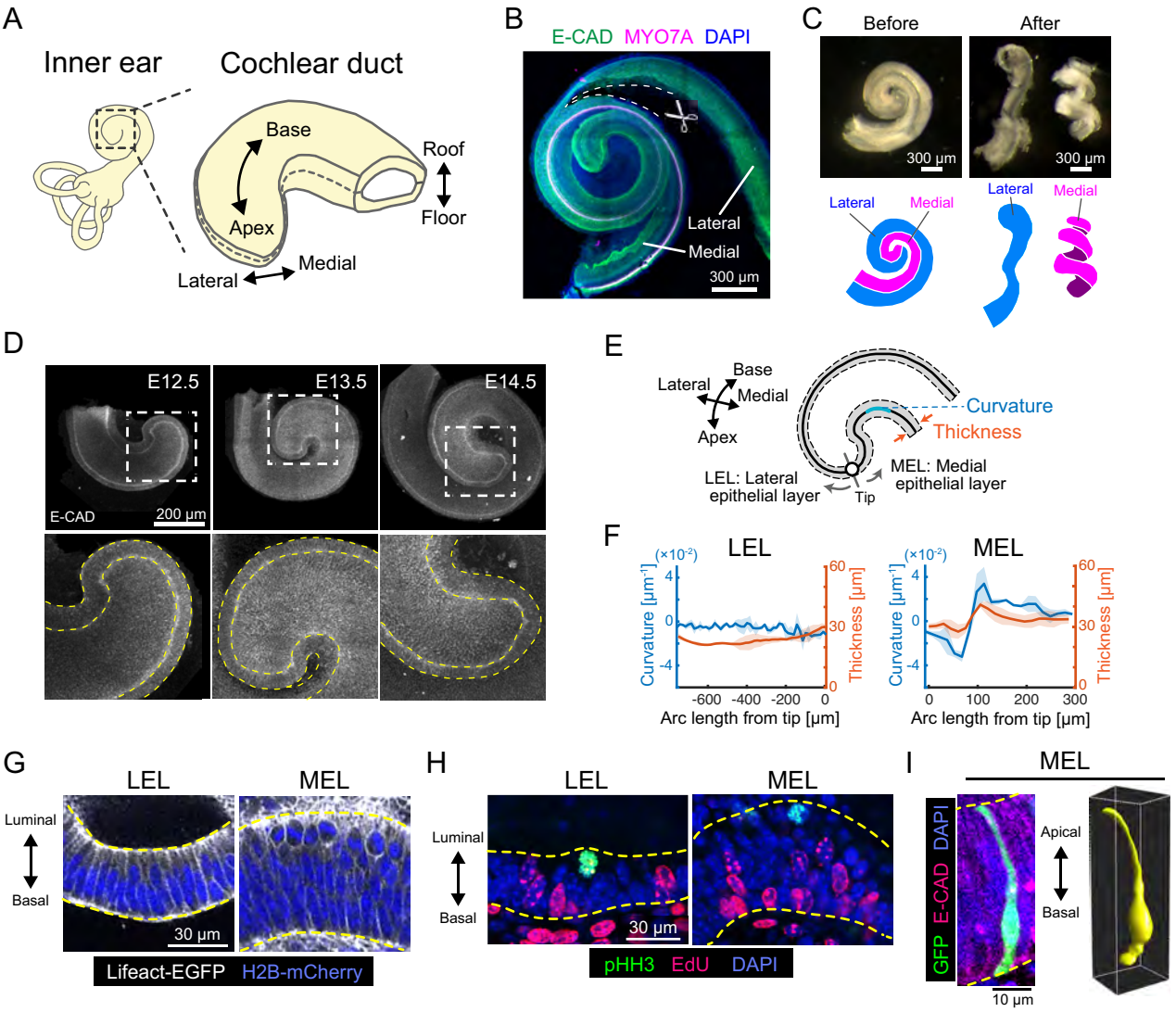

Figure 2

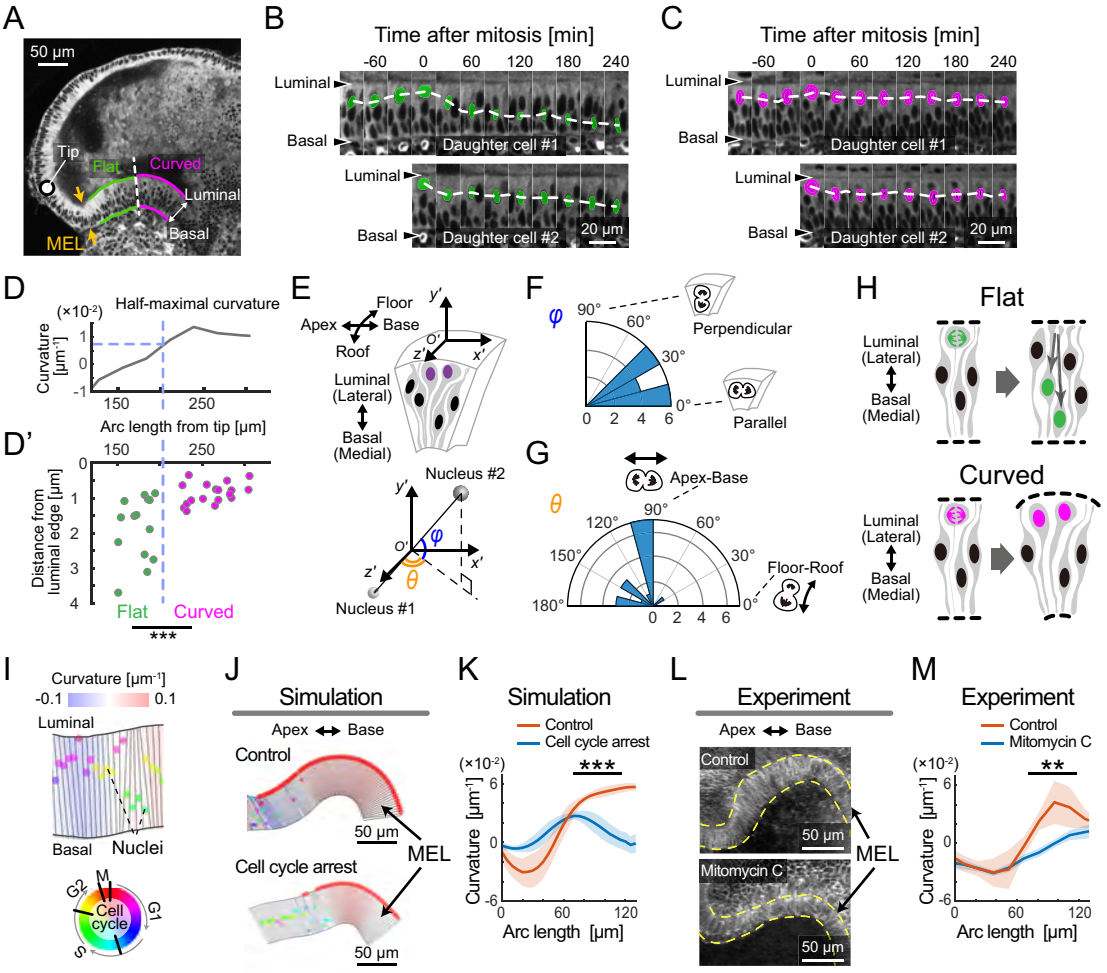

Figure 3

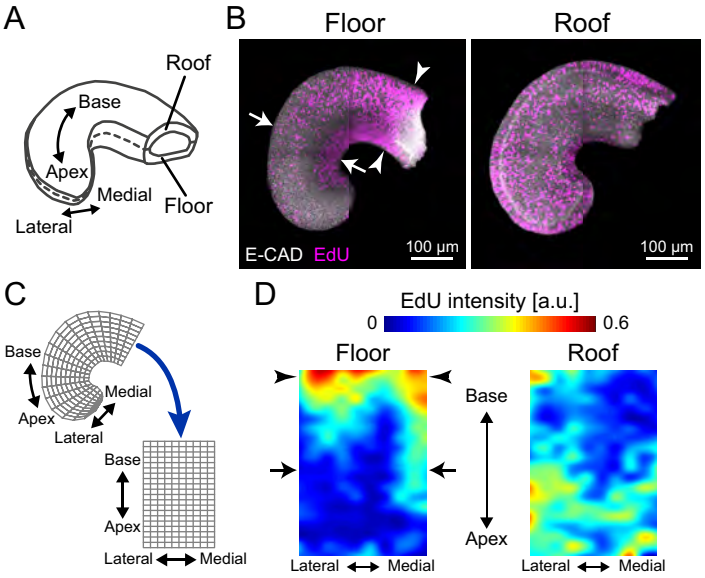

Figure 4